Powder Technology 407 (2022) 117540

Contents lists available at ScienceDirect

Powder Technology

journal homepage: www.journals.elsevier.com/powder-technology

Reduction kinetics of combusted iron powder using hydrogen

C.J.M. Hessels [a], T.A.M. Homan [a,b], N.G. Deen [a,b], Y. Tang [a,b,*]

[a] Department of Mechanical Engineering, Eindhoven University of Technology, the Netherlands
[b] Eindhoven Institute for Renewable Energy Systems (EIRES), Eindhoven University of Technology, the Netherlands

HIGHLIGHTS

- The reaction of combusted iron powder with hydrogen is studied.
- A new kinetic analysis method is proposed for analyzing multistep reactions.
- Final pore size is dependent on temperature, but not on hydrogen concentration.
- A multistep mechanism is needed to describe reduction at high temperature.

GRAPHICAL ABSTRACT

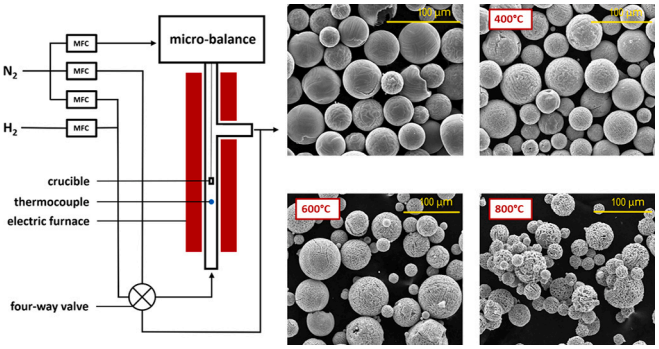

ARTICLE INFO

Keywords:
Thermogravimetric analysis
Metal fuels
Direct reduced iron
Hydrogen
Reduction kinetics
Iron powder

ABSTRACT

Despite extensive research on reduction of iron oxides in literature, there is no consensus on the most accurate reduction kinetics, especially for micron-sized iron oxide powders with high purity. Such data is particularly important for the application of metal fuels and chemical looping combustion, in which high purity iron powders function as dense energy carriers. Hence, in this work, hydrogen reduction of iron oxide fines, produced by iron combustion, were investigated using thermogravimetric analysis (TGA). The isothermal reduction experiments were conducted at the temperature range of 400–900 °C and at hydrogen partial pressures of 0.25–1.0 atm. Scanning electron microscopy (SEM) showed that the morphology of the reduction products depends on the reduction temperature but not on the hydrogen partial pressure. Reduction at higher temperatures leads to larger pore sizes. Based on an extended Hancock-Sharp "lnln"-method the appropriate gas-solid reaction models are determined, suggesting that the reduction can be described by a single-step phase boundary controlled reaction at temperatures below 600 °C, whereas a multistep mechanism is required for the description of reactions at higher temperatures.

1. Introduction

Reduction of iron oxides has been extensively studied and reported in literature, owing to its importance for the steel-making industry. Different reducing agents have been investigated, including coke (conventional blast furnace), syngas and hydrogen (direct reduced iron

* Corresponding author at: Department of Mechanical Engineering, Eindhoven University of Technology, the Netherlands.
E-mail address: y.tang.2@tue.nl (Y. Tang).

https://doi.org/10.1016/j.powtec.2022.117540
Received 3 January 2022; Received in revised form 29 March 2022; Accepted 18 May 2022
Available online 27 May 2022

Table 1
Summary of kinetic studies on iron oxide reduction by hydrogen found in literature.

Reference	Material	Particle size (μm)	Reduction step	T-range (°C)	Model	E_a (kJ/ mol)	Reactor type
[13]	Limonite ore	44–89	$Fe_2O_3 \rightarrow Fe$	700–900	1D nucleation and growth + diffusion of oxygen in the dense iron layer	51	Rotary drum reactor
[14]	Taconite ore	20–53	$Fe_3O_4 \rightarrow Fe$	1300–1550	1D nucleation and growth	193	Drop tube reactor
[15]	Hematite ore	45–125	$Fe_2O_3 \rightarrow Fe$	1375–1475	Diffusion of Fe^{3+}-ions in the liquid product layer	156	Drop tube reactor
[16]	Magnetite ore (Pokphur)	75–180	$Fe_3O_4 \rightarrow Fe$	700–1000	Pore diffusion kinetics	42 & 55	Thermogravimetric analyzer
[17]	Hematite & limonite ore	250–500	$Fe_2O_3 \rightarrow Fe$	600–800	Nucleation and growth model	15–60	Fluidized bed reactor
[18]	Hematite ore (PEA Ridge Iron Ore Co.)	91	$Fe_2O_3 \rightarrow FeO$	700–900	Nucleation and growth + diffusion controlled	58.13	Thermogravimetric analyzer
[19]	Magnetite ore (Mesabi Range, USA)	4–40	$Fe_3O_4 \rightarrow Fe$	400–900	Nucleation and growth	65–70	Thermogravimetric analyzer
[20]	Hematite powder (Merck)	1–2	$Fe_2O_3 \rightarrow Fe_3O_4$	220–680	Nucleation and growth + phase boundary reaction	76	Thermogravimetric analyzer
[20]	Hematite powder (Merck)	1–2	$Fe_3O_4 \rightarrow Fe$	220–680	Nucleation and growth + phase boundary reaction	39–88	Thermogravimetric analyzer
[21]	Magnetite powder	1–2	$Fe_3O_4 \rightarrow Fe$	210–950	Diffusion	44–200	Thermogravimetric analyzer
[22]	Hematite concentrate (LKAB)	–	$Fe_2O_3 \rightarrow Fe$	350–750	–	70–166	Thermogravimetric analyzer
[23]	Hematite concentrate	–	$Fe_2O_3 \rightarrow Fe_3O_4$	21–900	1D nucleation and growth	89	Thermogravimetric analyzer
[23]	Hematite concentrate	–	$Fe_3O_4 \rightarrow Fe$	21–900	Nucleation and growth	70	Thermogravimetric analyzer

technique). Direct reduced iron (DRI), using syngas instead of coke, has seen a steady increase in production capacity, but is still a minor player [1]. In view of climate change, however, it is becoming more and more urgent to develop and improve on clean alternatives for iron production [2]. Therefore, research on DRI using solely hydrogen as the reducing agent has re-emerged and steadily increased in recent years [3–5].

Meanwhile, an increasing interest has arisen on hydrogen reduction of iron oxides, due to the recently emerging subject of metal fuels [6–11]. Hereby, iron powder is cyclically combusted and reduced, creating a dense energy carrier with advantages over batteries and hydrogen in respect of energy density and safety. Hydrogen is considered to be one of the prime reduction agents for the reduction process in this metal fuel cycle, since it can be produced from renewable energies via electrolysis. For the development of an efficient metal fuel cycle, it is important to understand the reduction kinetics of iron oxides resulting from the combustion process.

Finally, chemical looping combustion and chemical looping reforming are also examples of industrial processes, which often employ iron(oxides) as a carrier material [12]. Although chemical reactions involved are slightly different, they often operate in the same temperature range and similar reactors are envisioned for the metal fuel cycle. For the design of these processes, the reduction kinetics of fine iron oxides with high purity are also required.

Many experimental studies have been reported to investigate the reaction mechanism and kinetics of direct iron reduction by hydrogen. Some representative references are listed and compared in Table 1. The majority of these studies were based on naturally found iron ores. Wei et al. [13], for instance, used limonite ore obtained from Taiyuan Heavy Industry CO., Ltd. (China). They found that the reduction of hematite ore (Fe_2O_3) to metallic iron (Fe) in their rotary drum reactor was controlled by one-dimensional formation and growth of nuclei below 850 °C, while at 900 °C the reaction was mixed controlled with diffusion limiting the reaction in the final stages of the reduction. They found that the activation energy of the reduction process (described by a single step reaction) was 51 kJ/mol. Elzohiery et al. [14] used taconite ore fines (20–53 μm) of the Mesabi range (U.S.) in their high temperature (1150–1350 °C) drop tube reduction experiments. They found that they could reduce their samples within several seconds and the conversion rate could best be described by one dimensional nucleation and growth with an activation energy of 193 kJ/mol. They also found that reduction had a first-order dependency on the hydrogen partial pressure. In their case, the effect of particle size was found to be negligible within their studied range. Similar type of experiments (high temperature drop tube) were also performed by Qu et al. [15] but using a different type of ore (with a similar particle size). They found that their experimental results could best be described by a 3D phase boundary reaction (shrinking core model). The apparent activation energy of this reaction was 270 kJ/mol in the temperature range 1277–1477 °C. Kuila et al. [16] used Indian magnetite ore from Pokphur in the Kiphere district of Nagaland. Their experiments showed that the reduction of these fines (75–180 μm) between 700 and 1000 °C took place in two stages. The magnetite is first reduced to wüstite and afterwards the wüstite is further reduced to metallic iron. The activation energies of the two stages were found to be 42 and 55 kJ/mol, respectively. Spreitzer and Schenk [17] performed reduction experiments on four different kinds of ores in the temperature range of 600–800 °C. They used a combination of three parallel nucleation and growth models, which were able to describe all four different ores. However, the calculated apparent activation energies varied in the range 15–60 kJ/mol depending on both the type of ore and the degree of reduction. Piotrowski et al. [18] reduced fine (91 μm mean diameter) hematite powder (PEA Ridge Iron Ore Co.) to wüstite in the range of 700–900 °C. They found that the reduction could best be described by a nucleation and growth model for the initial stage of the reduction, which later switched to a 1D diffusion model. The nucleation and growth model had an apparent activation energy of 58 kJ/mol. Morales-Estrella et al. [19] used magnetite concentrated ore from the Mesabi Range (U.S.) and performed reduction experiments using hydrogen in the temperature range of 400–900 °C. They studied both standard and activated (milled) powder. They found that sintering occured above 700 °C and therefore they only derived kinetic parameters for the temperature range of 400–500 °C. They found that the milled powder (which had a smaller mean particle size) had a higher conversion rate. Their data could be best fitted by a nucleation and growth model with an exponent of 2.5. They concluded that lattice strain due to the milling had an effect on the apparent activation energy, which was 70 kJ/mol for the as-received powder and 65 kJ/mol for the milled powder.

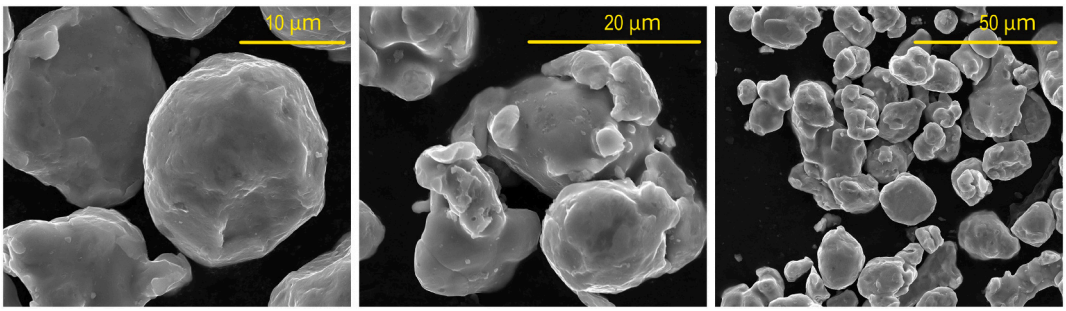

Fig. 1. SEM images of the high purity iron powder before the combustion process.

Natural iron ores possess large variation in size, composition and impurities, giving a partial cause to the spread in the kinetic parameters obtained in above-mentioned studies. In contrast, some studies have been performed for (synthetic) iron oxides with high purity. Pineau et al. [20,21] did research on low temperature reduction of hematite and magnetite reduction using high purity oxides (>99.8%). They found magnetite reduction occurred via 1D nucleation and growth or phase boundary reaction at temperatures below 650 °C, while diffusion was limiting for higher temperatures (measurements where performed up to 950 °C). Hematite to iron reduction was found to be best described by a nucleation and growth model below 420 °C, while it is controlled by the phase boundary reaction at higher temperatures (up to 680 °C). Pourghahramani and Fossberg [22] used high purity hematite concentrate and found that the reaction occurs in a two step process (from hematite to magnetite to iron). They analyzed the reduction using a model free method in the temperature range 350–750 °C. The determined apparent activation energy showed a strong dependence on the extent of conversion, indicating a mixed control regime. Lin et al. [23] prepared their hematite sample by precipitating a $Fe(NO_3)_2{\cdot}9H_2O$ solution from Fisher Chemical Corporation. They found that the reduction behavior could best be described by a two step mechanism. The hematite to magnetite reduction matched best with a uni-molecular model (E_a = 89.13 kJ/mol), while the magnetite to metallic iron matched best with a 2D nucleation model (E_a = 70.41 kJ/mol). The size of the powder used in [20,21] is around 1–2 µm, and was unfortunately not reported in [22,23].

As shown in the aforementioned studies, even for high purity iron oxides, the reduction kinetics varies significantly due to the influence of macro-structure (particle size, porosity) and micro-structure (crystalline size, vacancies, impurities), as well as the experimental conditions (temperature, methods). This has also been pointed out by other researchers [21,24–26]. Due to this large spread of results in literature, there currently exists no generic kinetic model nor fixed parameters for iron oxide reduction. New types of materials therefore require their own kinetic measurement and analysis. The iron oxide powder for the application of metal fuel has unique characteristics, e.g., composition, size, surface morphology etc., for which, to the authors' knowledge, no study has been reported yet in literature.

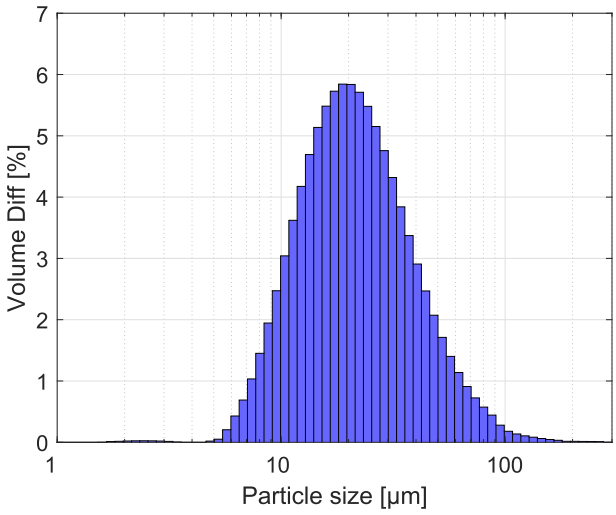

Fig. 3. Particle size distribution (volume based) of combusted iron powder used in this research.

This work therefore aims to derive the reduction kinetics of iron oxides using hydrogen with respect to this aforementioned metal fuel application. The iron oxides studied are direct products of iron combustion. The conversion rate of the powders is studied using isothermal thermogravimetric experiments at temperatures between 400 and 900 °C and hydrogen partial pressures of 0.25–1.0 atm. The weight loss of the powder is recorded and converted into a conversion rate. Based on an extended Hancock-Sharp "lnln"-method [27] the appropriate gas-solid reaction models are determined, which are then fitted to the experimental data to obtain the kinetic parameters.

This paper is organized as follows: First, the materials and methods used are described, after which the kinetic analysis strategy is explained. Subsequently, the experimental results are given, followed by the kinetic analysis of these results and conclusions of the presented work.

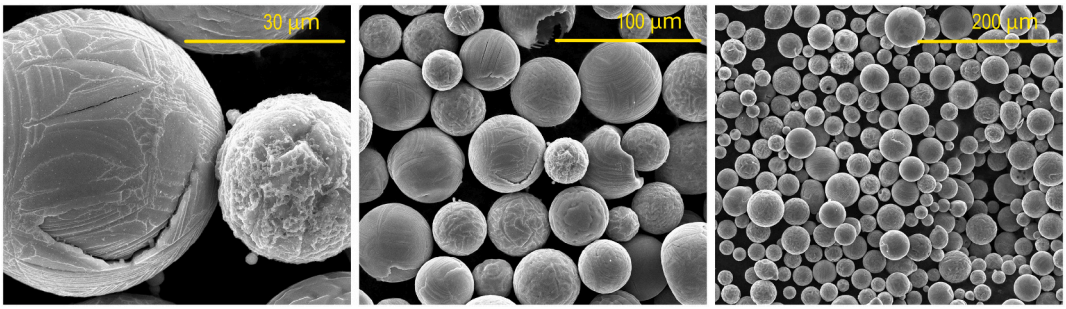

Fig. 2. SEM images of the iron oxide powder after the combustion process.

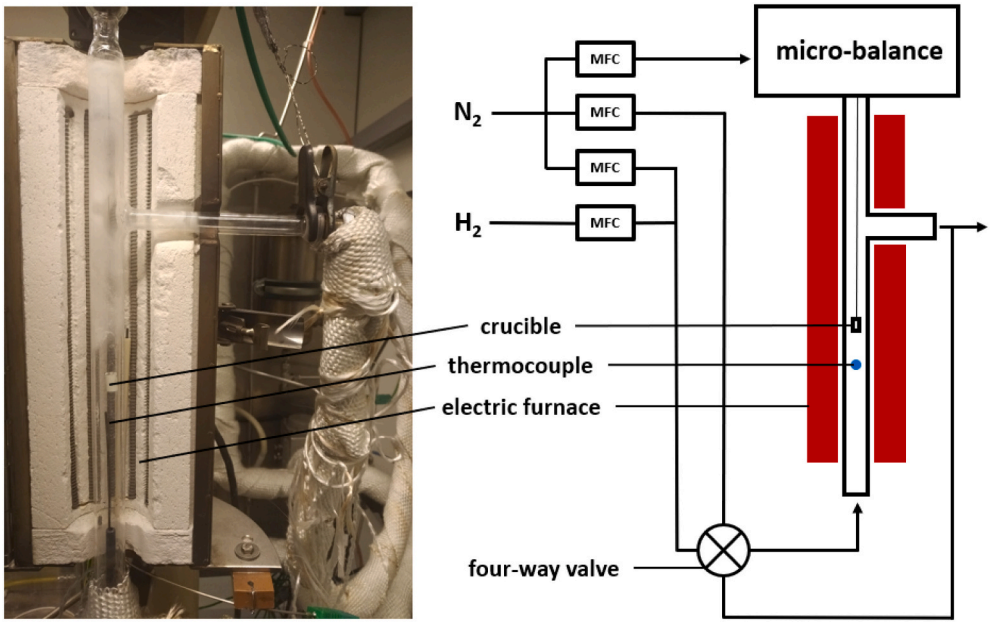

Fig. 4. Photograph and schematic diagram of the thermogravimetric analyzer.

2. Materials and methods

2.1. Materials

The iron oxide powder used in this study is produced by combustion of high purity (99% Fe) iron powder from CNPC Powder (CNPC-FE400) in an in-house developed cyclonic burner [28]. While the exact combustion process is still a topic of active research [11,29–41], studies suggest that during the combustion process the iron powder melts and the molten iron droplets react with oxygen. They solidify in the burner exhaust and are captured using a cyclone. As a result, the iron oxide powder consists of predominantly spherical particles. SEM images (made with a FEI Quanta 600) of the powder before and after combustion can be seen in Figs. 1 and 2, respectively. The particle size distribution of the combusted powder, determined using the laser diffraction method (Malvern Mastersizer 2000), is given in Fig. 3. The specific surface area, estimated from this particle size analysis, is 330 m^2/kg. The bulk density was estimated using a measuring cylinder to be 3287 kg/m^3, resulting in a particle density of 5193 kg/m^3, assuming close random packing.

X-ray powder diffraction showed that the oxide powder consisted of about 40 wt% hematite (Fe_2O_3), 58 wt% magnetite (Fe_3O_4). The other 2 wt% is made up of traces of wüstite (FeO) and iron (Fe). Due to the high purity of iron powder used in the combustion process (99 wt% Fe), no other minerals are present in noticeable amount.

2.2. Thermogravimetric analyzer

TGA measurements are conducted using a thermogravimetric analyzer as seen in Fig. 4. The setup was initially developed in the work of Coenen et al. [42]. It consists of an aluminum-oxide crucible (5 mm inner diameter, 10 mm height and 1 mm wall thickness), suspended within a quartz tube, which in turn is surrounded by electric heating elements. The quartz tube is on the top connected to a micro-balance (CI-Precision MK2-5 M) with a sensitivity of 0.1 μg, from which the crucible is suspended. A flow of nitrogen is supplied from the balance side, to prevent reactive gases from entering the balance. On the bottom side of the quartz tube, a mixture of reducing and non-reducing gases can be supplied. All mass flows are controlled by Bronkhorst mass flow controllers (MFC). A thermocouple (type K) is placed just below the crucible, to measure the local temperature and to control the heating elements.

2.3. Experimental procedure

During each experiment the crucible, filled with around 150 mg of iron oxide powder, is placed in the setup and is heated at a controlled rate of 20 °C per minute. During heat-up, nitrogen is supplied, with a flow rate of 0.5 NLPM (reference conditions: 0 °C and 1.0 atm) to prevent the powder from further oxidizing. When the required temperature is reached, the flow is switched to a set mixture of hydrogen and nitrogen. The mass flow rates during these experiments, were: 0.48 NLPM H_2 and 0 NLPM N_2 for the 1.0 atm. H_2 experiments, 0.4 NLPM H_2 and 0.4 NLPM N_2 for the 0.5 atm. H_2 experiments, and 0.15 NLPM H_2 and 0.45 NLPM N_2 for the 0.25 atm. H_2 experiments. After the set reduction time is reached, the powder is cooled down (also 20 °C/min), again in a nitrogen environment (0.5 NLPM). During the entire process, the flow rates of the gases, the temperature and the mass of the crucible are recorded each second. The crucible is also weighed before and after the experiment, both with and without powder. The conversion of the powder at any time is defined as:

$$X(t) = \frac{m_0 - m(t)}{m_0 - m_{0\rightarrow\text{iron}}}, \tag{1}$$

where m_0 is the original mass of the powder, $m(t)$ is the recorded mass at time t and $m_{0\rightarrow\text{iron}}$ is the theoretical mass of the sample assuming full conversion to metallic iron (using an initial composition of 40 wt% Fe_2O_3, 58 wt% Fe_3O_4 and 2 wt% Fe).

2.4. Kinetic analysis

In general, the conversion rate of a gas-solid reaction can be defined as:

$$\frac{dX}{dt} = k_{app}(T) f(X), \tag{2}$$

in which $k_{app}(T)$ contains the temperature dependency of the conversion rate (constant in an isothermal experiment) and $f(X)$ is a function describing the influence of the conversion extent on the conversion rate. Rate constant $k_{app}(T)$, often follows the Arrhenius equation:

Table 2
Mathematical models describing the conversion rate dependency on the conversion.

Model	Abbreviation	**g(X)**
Internal diffusion controlled	IDM	$1-3\,(1-X)^{2/3}+2\,(1-X)$
Phase boundary controlled	PBC	$1-(1-X)^{1/3}$
Nucleation and growth	NAG	$-\ln(1-X)^{1/n}$

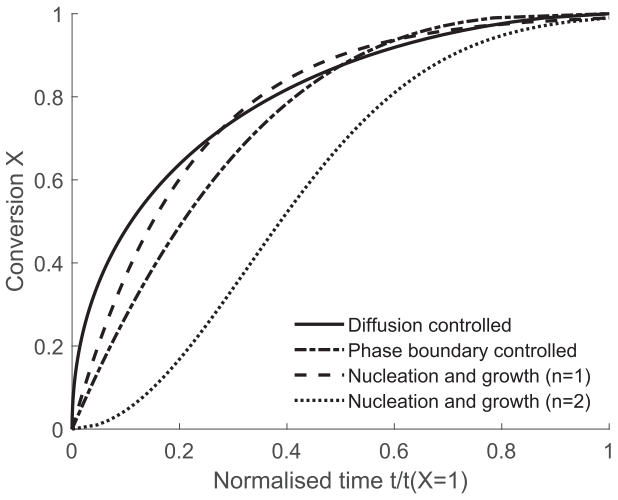

Fig. 5. Characteristic shapes of mathematical models $g(X)$ of Table 2.

$$k_{app}(T) = k_{app,0} exp\left(-\frac{E_a}{RT}\right), \tag{3}$$

with R the universal gas constant, $k_{app,0}$ the pre-exponent factor and E_a the apparent activation energy. $k_{app,0}$ and E_a and $f(X)$ are together also known as the kinetic triplet of gas-solid reactions.

Three common methods exist for extracting the kinetic parameters, each having its own respective advantages and disadvantages. These methods are (1) the model fitting method, (2) the isoconversional method and (3) the "lnln" method. The methods are briefly described below.

Different mathematical expressions exist for $f(X)$ based on theoretical kinetic models. Moreover, by integrating Eq. 2 in time we obtain:

$$g(X) = \int_0^X \frac{1}{f(X)} dX = k_{app}(T)\cdot t \tag{4}$$

The most common expressions for $g(X)$ for gas-solid reactions of spherical particles are given in Table 2.

From Eq. 4 we can conclude that by plotting $g(X)$ as a function of time, we should obtain a straight line, assuming the correct kinetic model is used. Linear regression can thus be used to decide which model best describes the experimental data. This method is often referred to as the model fitting method.

This method however is often also criticized, since multiple models might have a similar shape. This can be observed in Fig. 5 in which the diffusion model, the phase boundary model and the 1D nucleation and growth model show a similar shape. Fitting any of these models to experimental results may result in a satisfying fit, especially when taking measurement errors into account.

Isoconversional methods overcome this issue by deriving a value for the activation energy as function of the reduction degree. Assuming that the controlling mechanism is not dependent on temperature, at a given value of X, $f(X)$ is constant. Therefore, by performing multiple experiments at different temperatures, E_a can be derived as function of conversion X. A drawback of this method is that it can only be used to derive a value for the activation energy if $f(X)$ does not change as function of the temperature. In the case of mixed controlled reactions (both mass transfer and reaction kinetics are of importance), this assumption usually does not hold (since they scale differently with temperature). The same holds when the reaction consists of multiple reaction steps with intermediate species.

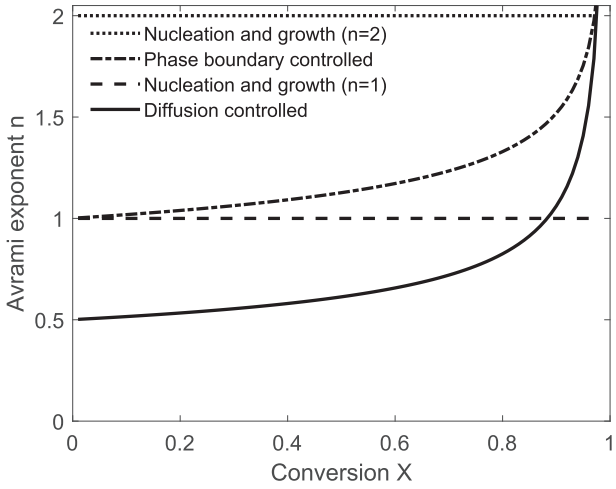

Fig. 6. Avrami exponent n as function of conversion extent X for the different mathematical models $g(X)$ of Table 2.

The third method for analyzing gas-solid reaction was developed by Hancock and Sharp [27]. They noticed that, when only taking into account the data between $0.15 < X < 0.5$ all common kinetic models ($f(X)$) could also be described by the nucleation and growth model, if the value of n is used as a fitting parameter (instead of the traditionally used integer values). They suggested to determine the value of n by plotting $\ln(-\ln(1-X))$ vs $\ln(t)$, since the result would give a straight line with a slope of n:

$$g(X) = -ln(1-X)^{1/n} = k_{app}(T)\cdot t \tag{5}$$

$$ln(-ln(1-X)) = n\cdot ln\left(k_{app}(T)\right) + n\cdot ln(t) \tag{6}$$

$$\frac{dln(-ln(1-X))}{dln(t)} = n \tag{7}$$

Based on the value of n, a suggestion can be made on whether the reaction is reaction or diffusion controlled. A drawback is that one only fits their model to the conversion between 0.15 and 0.5, neglecting data outside that range.

It is well known that the reduction of iron oxides consist of multiple step reactions [20]:

$Fe_2O_3 \rightarrow Fe_3O_4 \rightarrow Fe$ (below 570 °C)

$Fe_2O_3 \rightarrow Fe_3O_4 \rightarrow FeO \rightarrow Fe$ (above 570 °C)

Due to the drawbacks of the first two methods (especially in the case of multi-step reactions), in this study, an extended version of the Hancock and Sharp method is used in combination with the model fitting method to analyze the reduction behavior of the oxides. Instead of plotting $\ln(-\ln(1-X))$ vs $\ln(t)$, the value of n (often called the Avrami exponent) is plotted as a function of the conversion X. The resulting curves for the various mathematical models in Table 2 are plotted in Fig. 6.

Comparing Figs. 5 and 6 it is observable that models in Fig. 5 with a similar shape are now well distinguishable.

3. Experimental results

Isothermal TGA tests were performed at different temperatures between 400 °C and 900 °C and hydrogen partial pressures between 0.25 atm and 1.0 atm.

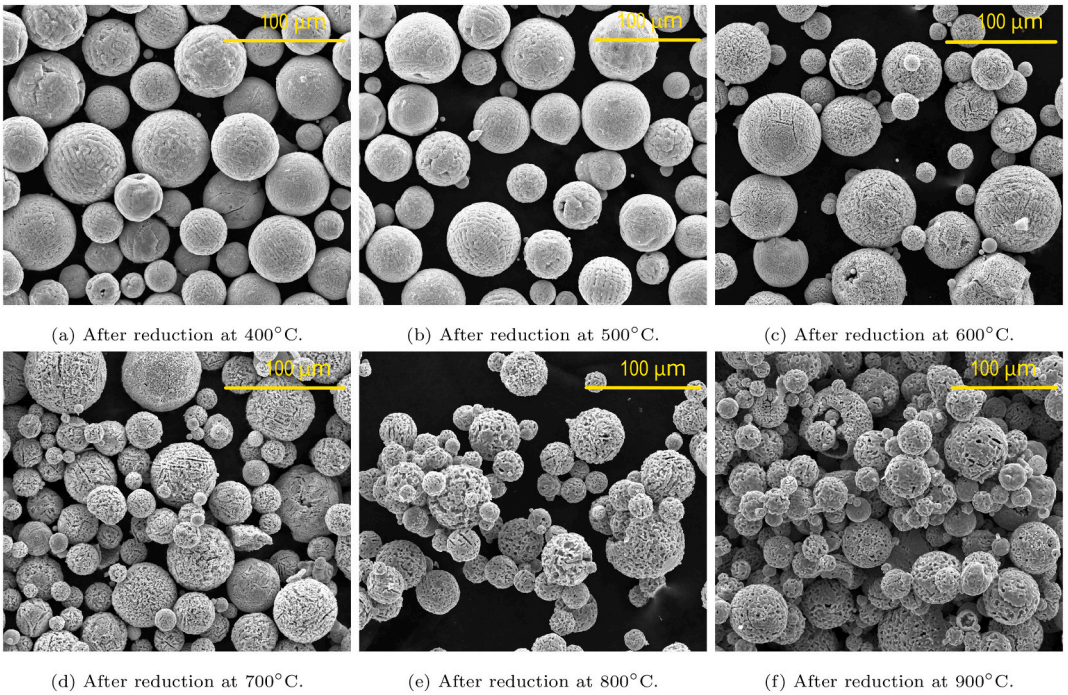

(a) After reduction at 400°C. (b) After reduction at 500°C. (c) After reduction at 600°C.

(d) After reduction at 700°C. (e) After reduction at 800°C. (f) After reduction at 900°C.

Fig. 7. Scanning electron microscope images of iron oxide after reduction at various temperatures. Note that there are small differences in the magnification used in the images.

3.1. Morphological observations

Fig. 7 shows electron microscope images of the powder after reduction at different temperatures. Different hydrogen partial pressure did not lead to differences in the morphology of the sponge iron formed. Therefore, all SEM images presented are from powder reduced at a hydrogen partial pressure of 0.5 atm. Compared to the original oxides as seen in Fig. 2, it can be observed that the powder becomes porous in all reduction experiments. The pore structure, in particular the average pore size, differs between experiments at different temperatures. As the reduction temperature increases, the number of pores decreases, but the pore size increases. This observation matches with the findings of Turdogan [43].

It should be noted that, although swelling and shrinkage of particles has been mentioned in literature [44,45], no clear sign of particle size change could be identified from the SEM images.

Furthermore, at temperatures above 500 °C, agglomeration of the powder was found to occur in the experiments. As temperature increased, this effect gradually became stronger. This agglomeration might have to do with the formation of wüstite as an intermediate species, which is only stable above 570 °C.

3.2. Reduction behavior

Fig. 8 shows the evolution of conversion extent of iron oxide for different temperatures and hydrogen partial pressures. Each graph represents experiments performed at a fixed temperature, where each line in the graphs represents an experiment at a specific hydrogen partial pressures. The line markers are only used for visualization purposes, since the weight of the samples is recorded at each second during each experiment. In each graph, reference lines are added to show at which points there would be full conversion to magnetite (dashed), wüstite (dotted) and metallic iron (dash-dotted), ideally if the reactions take place step-by-step. If any of the intermediate reactions ($Fe_2O_3 \rightarrow Fe_3O_4$, $Fe_3O_4 \rightarrow FeO$ or $FeO \rightarrow Fe$) would take place at a much faster reaction rate compared to the subsequent ones, a clear change in the conversion rate would be observed when the reference lines are crossed. Since no clear transition can be observed, this conclusion cannot be drawn.

It can be observed that at all temperatures a higher hydrogen partial pressure leads to a faster conversion rate, as expected. Only for reduction at 800 °C the effect of hydrogen partial pressure is different. Initially, a higher hydrogen partial pressure leads to higher conversion in the same amount of time. However, when the experiment is ran for longer time we observe that the conversion extent at 1.0 atm of hydrogen partial pressure stagnates, while for 0.5 atm it keeps increasing. After 70 min, the powder reduced at 0.5 atm H_2 reaches a higher conversion than reduction at 1.0 atm H_2. This effect is not observed in the other experiments. A possible explanation for this is that of strong agglomeration occurring, coincidentally leading to this effect.

When comparing reduction curves at different temperatures (with fixed hydrogen partial pressure) we can observe that the initial conversion rate increases with temperature. However, while at reduction temperatures between 400 and 600 °C the curves seems to “smoothly” reach to a full conversion, at higher temperatures (700–900 °C) a distinct transition is observable. Initially the conversion rate is fast, but starting from a conversion extent of 0.5–0.6, the conversion rate sharply decreases. In some cases, full conversion is not even reached within the 2 h time frame of the experiments. Similar observations have been reported in other studies. Piotrowski et al. found a similar decrease in conversion rate [18]. They suggested that the sharp decrease was due to solid state diffusion becoming the limiting factor. Their suggestion agrees with the model of Qu et al. [46], in which solid state diffusion of oxygen becomes rate-limiting in the later stage of the reduction.

Another possible explanation for this transition might be agglomeration of the powder. As mentioned before, agglomeration of the powder took place at experiments between 600 and 900 °C. This agglomeration might hinder mass transfer of hydrogen between particles and thus decrease the conversion rate. Similar agglomeration effects were observed by Morales-Estrella et al. [19]. For the case of 900 °C and 1.0 atm of hydrogen, the conversion rate goes above 1. This is most likely

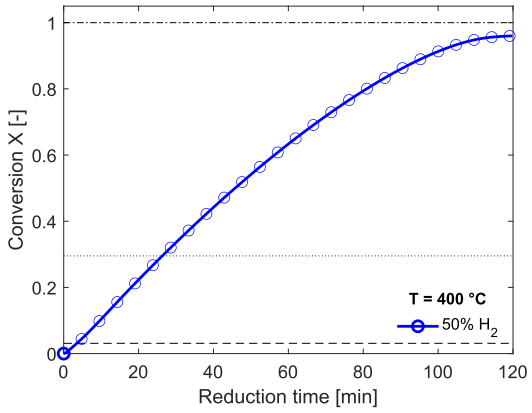

(a) Reduction at a temperature of 400°C.

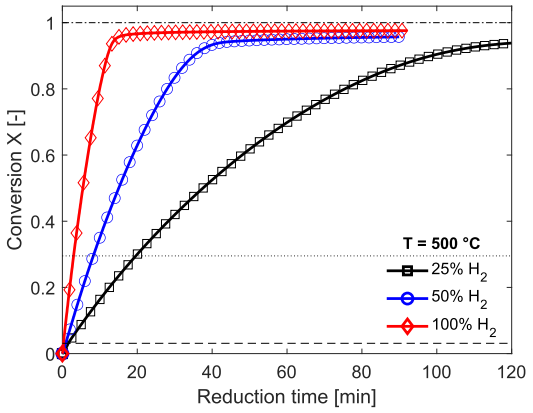

(b) Reduction at a temperature of 500°C.

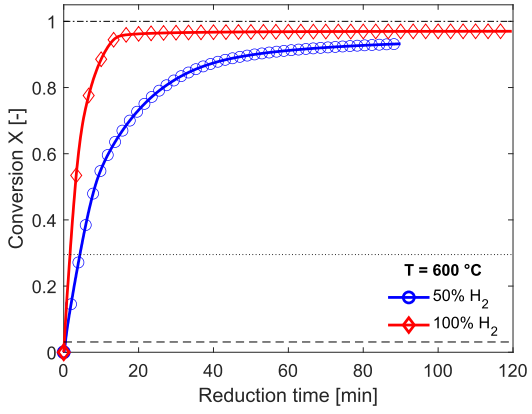

(c) Reduction at a temperature of 600°C.

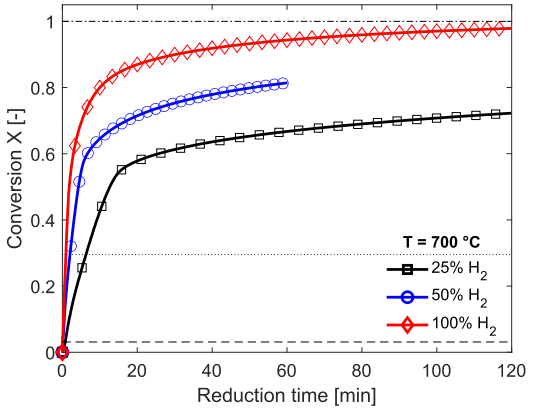

(d) Reduction at a temperature of 700°C.

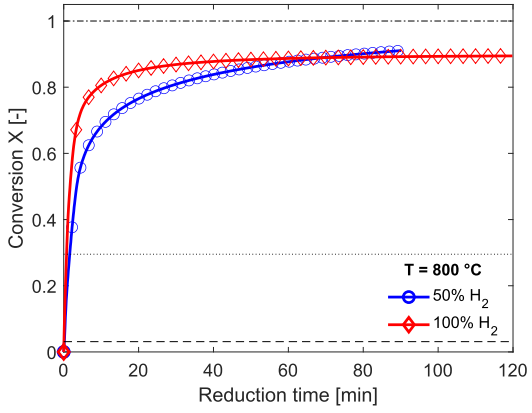

(e) Reduction at a temperature of 800°C.

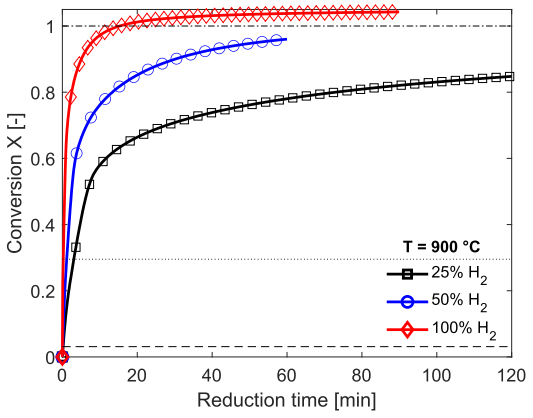

(f) Reduction at a temperature of 900°C.

Fig. 8. Influence of hydrogen gas concentration on iron oxide reduction at temperatures of 400–900 °C. The weight of the sample is measured at every second, which means that the markers are only added for visualization purposes. The black dashed, dotted and dash-dotted horizontal lines in the figure represent 100% conversion to magnetite, wüstite and metallic iron, respectively, if the reactions take place step-by-step.

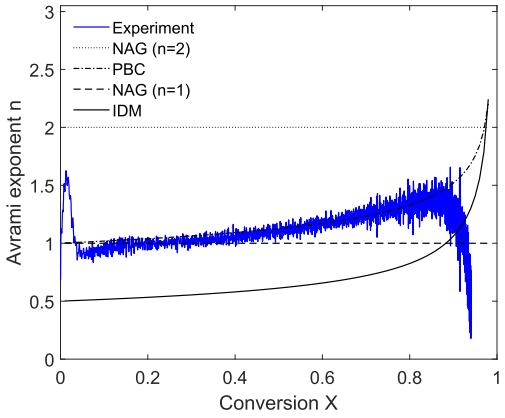

(a) Avrami exponent as a function of reduction degree for reduction at 500°C and a hydrogen partial pressure of 0.25 atm. The phase boundary model best matches with the experimental data.

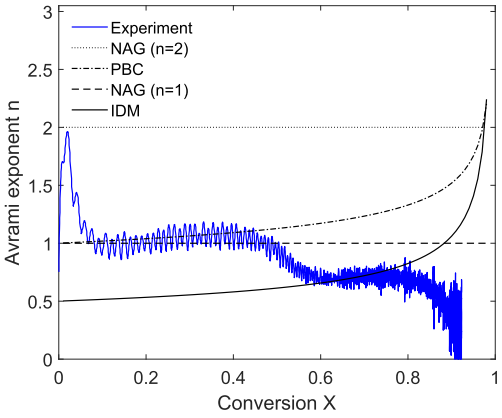

(b) Avrami exponent as a function of reduction degree for reduction at 600°C and a hydrogen partial pressure of 0.5 atm. In the lower stage of reduction ($X < 0.4$) the experimental data matches with the phase boundary reaction. However, the later stage ($0.6 < X < 0.8$) of the reduction has a sharp drop/decrease. This means that none of the models will be able to correctly describe the reaction.

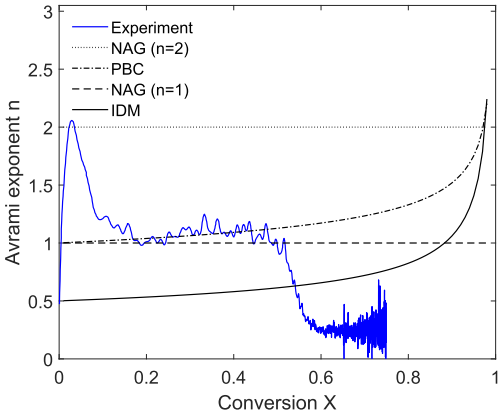

(c) Avrami exponent as a function of reduction degree for reduction at 700°C and a hydrogen partial pressure of 0.25 atm. In the lower stage of reduction ($0.15 < X < 0.5$) the experimental data matches with the phase boundary reaction, while in the later stage the value for the exponent drops significantly and does not match with any of the models.

Fig. 9. Extended Hancock and Sharp method for experiments at different temperatures.

the result of an error in the weighing of the powder or of the initial composition. A noteworthy effect of this decrease in conversion rate is that full conversion ($X = 1$) is reached faster at low temperatures (400–600 °C), than at higher temperatures (700–900 °C).

4. Kinetic results

As shown in Fig. 5, the standard model fitting method solely could not reveal the reaction mechanism. In fact, we found out that multiple models can fit the experimental data at lower temperatures equally well, whereas none of the models gives a satisfactory fit to the data at higher temperatures. The results of this standard model fitting method are presented in Appendix A. To better understand the reaction mechanism, the extended Hancock and Sharp method is first used to further analyze the experimental results and to improve the interpretation of the model fitting method.

4.1. Model selection

Fig. 9 shows the Avrami exponent for the cases of 500 °C, 600 °C and 700 °C. For the 500 °C case, it can clearly be observed that the data follows the phase boundary controlled model almost perfectly. The deviation of the experimental results at high conversion ($X > 0.8$) is due to small measurement errors in the sample weight and initial composition. The deviation at low conversion ($X < 0.05$) is most likely due to the conversion of hematite to magnetite. This step is generally known to be

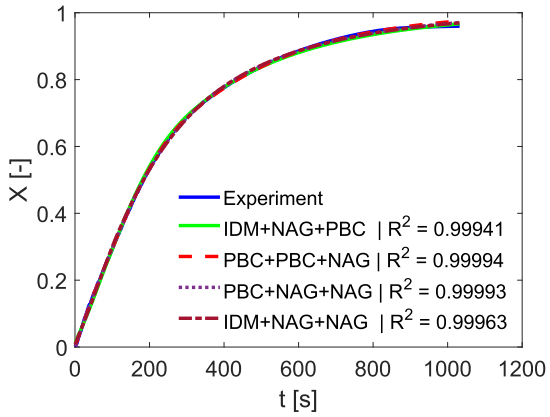

(a) Model fitting results of 4 different combinations of models, using a multistep mechanism.

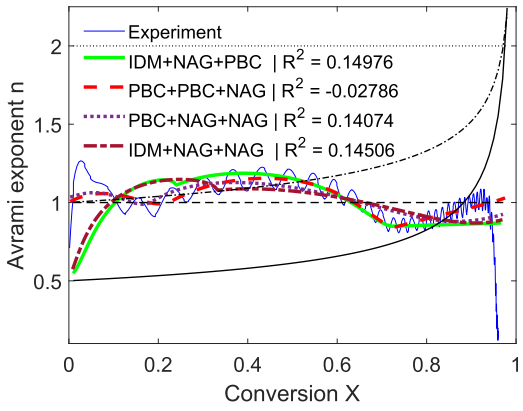

(b) Avrami exponent as a function of reduction degree.

Fig. 10. Fitting results at 600 ˚C and 1.0 atm hydrogen pressure using multistep kinetics. The legend entries describe the combinations of the models used for X_{hem}, X_{mag} and $X_{wüs}$.

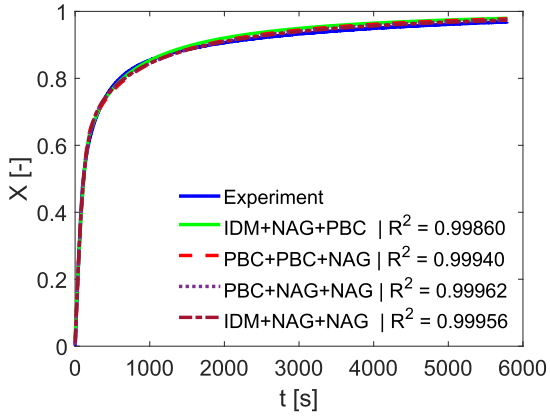

(a) Model fitting results of 4 different combinations of models, using a multistep mechanism.

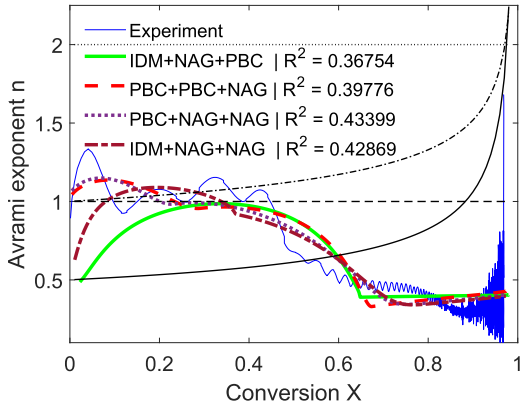

(b) Avrami exponent as a function of reduction degree.

Fig. 11. Fitting results at 700 ˚C and 1.0 atm hydrogen pressure using multistep kinetics. The legend entries describe the combinations of the models used for X_{hem}, X_{mag} and $X_{wüs}$.

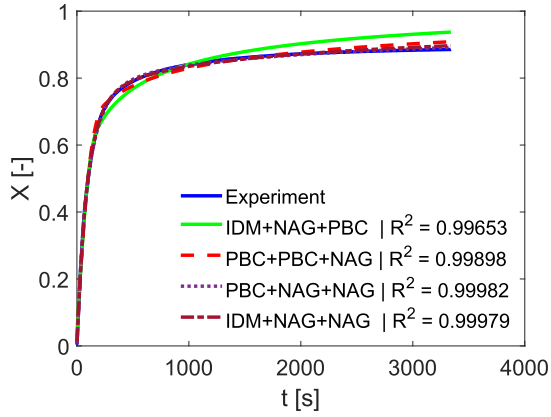

(a) Model fitting results of 4 different combinations of results, using a multistep mechanism.

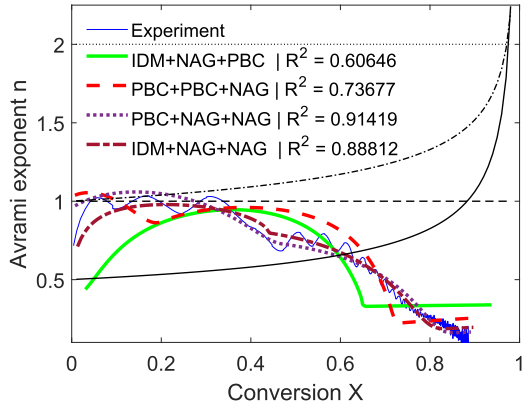

(b) Avrami exponent as a function of reduction degree.

Fig. 12. Fitting results at 800 °C and 1.0 atm hydrogen pressure using multistep kinetics. The legend entries describe the combinations of the models used for X_{hem}, X_{mag} and $X_{wüs}$.

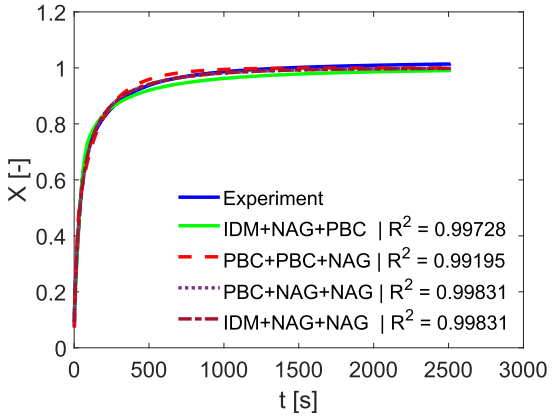

(a) Model fitting results of 4 different combinations of results, using a multistep mechanism.

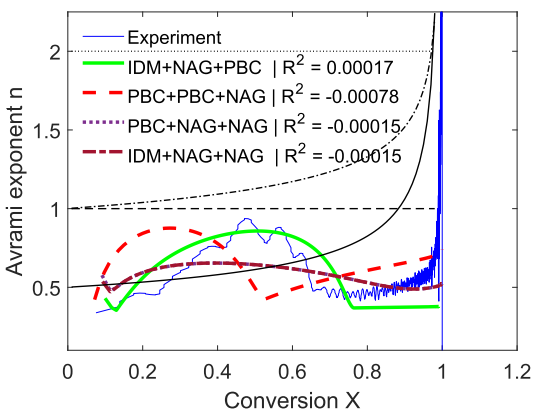

(b) Avrami exponent as a function of reduction degree.

Fig. 13. Fitting results at 900 °C and 1.0 atm hydrogen pressure using multistep kinetics. The legend entries describe the combinations of the models used for X_{hem}, X_{mag} and $X_{wüs}$.

significantly faster than the magnetite to iron reaction. However, since this conversion happens early on in the experiment, it is intertwined with stabilization of the hydrogen-nitrogen gas ratio. It is therefore difficult to obtain good kinetic data for this reduction step. The rest of the reaction follows a simple phase boundary reaction, often referred to as a reaction controlled shrinking core model. The low temperature experiments (400 and 500 °C) can therefore be evaluated by fitting a single phase boundary reaction:

$$X = 1 - \left(1 - k_{app} \cdot t\right)^3 \tag{8}$$

Evaluating the cases of 600 °C and 700 °C, it can be observed that the experimental data does not solely follow any of the single step analytical models. A clear transition can be observed at $X \sim 0.1$ and $X \sim 0.5$. This suggests a multi-step reaction mechanism is required to describe the reduction behavior at these higher temperatures.

4.2. Multi-step mechanism

To analyze the higher temperature reactions, a multi-step mechanism is required, to account for the intermediate species. Defining our initial masses of hematite, magnetite, wüstite and iron as $m_{hem,0}$, $m_{mag,0}$, $m_{wüs,0}$ and $m_{iron,0}$, respectively, and setting up the conservation of mass, we can define our masses at any time as:

$$m_{hem} = m_{hem,0} \cdot (1 - X_{hem}) \tag{9}$$

$$m_{mag} = \left(m_{mag,0} + \frac{2M_{mag}}{3M_{hem}} m_{hem,0} \cdot X_{hem}\right) \cdot (1 - X_{mag}) \tag{10}$$

$$m_{wüs} = \left(m_{wüs,0} + \frac{3M_{wüs}}{M_{mag}} \left(m_{mag,0} + \frac{2M_{mag}}{3M_{hem}} m_{hem,0} \cdot X_{hem}\right) \cdot X_{mag}\right) \cdot (1 - X_{wüs}) \tag{11}$$

$$m_{iron} = m_{iron,0} + \frac{M_{iron}}{M_{wüs}} \left(m_{wüs,0} + \frac{3M_{wüs}}{M_{mag}} \left(m_{mag,0} + \frac{2M_{mag}}{3M_{hem}} m_{hem,0} \cdot X_{hem}\right) \cdot X_{mag}\right) \cdot X_{wüs} \tag{12}$$

in which M_i stands for the molar masses of the different species and X_i is the conversion of intermediate reaction step. For each of these conversions, we can again choose the models listed in Table 2. The fractions 2/3 and 3/1 result from the stoichiometry between the different oxides (Fe_2O_3 to Fe_3O_4 and Fe_3O_4 to FeO, respectively). The total conversion (which we measure experimentally) can then be defined as:

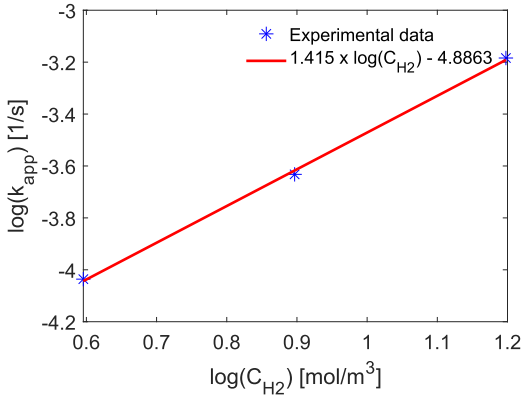

Fig. 14. Logarithmic graph of apparent reaction rate versus hydrogen concentration at 500 °C. Linear regression is used to determine the reaction dependency on hydrogen concentration.

$$X_{tot} = \frac{m_{tot,0} - m_{tot}}{m_{tot,0} - m_{tot,\infty}} \tag{13}$$

in which m_{tot} is the summation of the masses of hematite, magnetite, wüstite and iron and the subscripts $_0$ and $_\infty$ stand for initial mass and mass after full conversion (all X_i are 1).

To select the correct combination of models, the following assumptions are made:

- The reactions occur via a shrinking core principle, where the reaction leaves a shell of "lower" oxide and the reaction fronts travel inwards.
- In the case of an internal diffusion model, the diffusion of hydrogen towards the reaction front is limiting and the concentration of hydrogen goes to the equilibrium concentration when approaching the reaction front. This in combination with the previous assumption, means that only the first reaction step (hematite to magnetite) can be diffusion limited, with subsequent reactions (with reaction fronts closer to the surface of the particle), being only nucleation and growth or phase boundary controlled.
- Each reaction (X_i) can be described by one of the models from Table 2.

Different combinations of models are tested and the resulting fits are compared in both the conversion versus time and the "Avrami exponent"

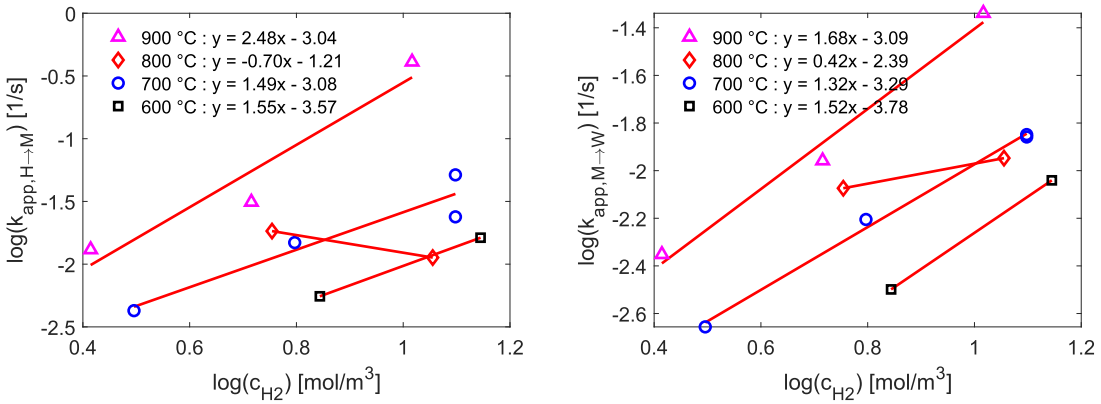

(a) Logarithmic graph of apparent reaction rate versus hydrogen concentration at various temperatures for the hematite to magnetite reaction step.

(b) Logarithmic graph of apparent reaction rate versus hydrogen concentration at various temperatures for the magnetite to wüstite reaction step.

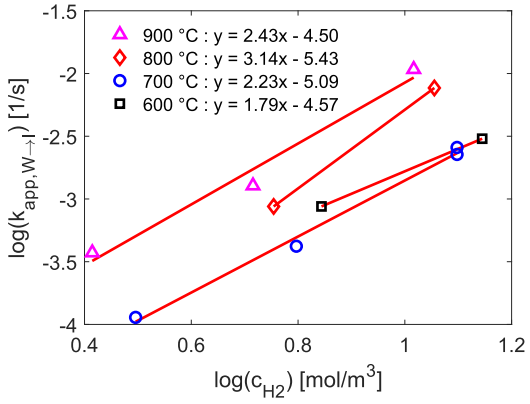

(c) Logarithmic graph of apparent reaction rate versus hydrogen concentration at various temperatures for the wüstite to iron reaction step.

Fig. 15. Dependency off the apparent reaction rates on the gas concentration for the elementary reaction steps of the high temperature multistep model.

Table 3
Apparent reaction rate, nucleation and growth exponent *n* and gas order *m* resulting from the single step (400–500 °C) and multistep (600–900 °C) analysis.

T [°C]	X_{tot}(PBC)							
	k_{app}(T)	m						
400	3.41E-06	1.42[1]						
500	1.30E-05	1.42						
	X_{hem}(PBC)		X_{mag}(NAG)			$X_{wüs}$(NAG)		
	k_{app}(T)	m	k_{app}(T)	n	m	k_{app}(T)	n	m
600	1.54E-04	1.55	1.65E-04	1.15	1.52	0.89E-04	0.86	1.79
700	3.61E-04	1.49	5.12E-04	1.2	1.32	0.93E-04	0.36	2.23
800[2]	2.62E-04	2[3]	2.62E-04	1.09	1.5[3]	2.62E-04	0.42	2.33[3]
900	2.45E-04	2.48	8.25E-04	0.97	1.68	2.65E-04	0.45	2.43

[1] The gas dependency at 400 °C is based on that at 500 °C.
[2] The kinetic parameters are based solely on the 0.5 atm. H_2 experiment.
[3] The gas dependency at 800 °C is based on the mean of 700 and 900 °C.

versus conversion graph. The results for higher temperature cases (600–900 °C) and 1.0 atm. H_2 are presented in Figs. 10-13. The coefficients of determination (R^2) are mentioned in the legend of the figures. It should be noted that the fitting occurs in the *X*, *t*-domain, while the Avrami exponent graph aids in selecting the correct model. Comparing the results, the conversion versus time graphs show all models fitting roughly equally well, as illustrated earlier. However, when looking at the Avrami exponent over conversion graphs, the models show more differences. The model that seems to fit all cases best, is the "PBC + NAG+NAG" model, meaning that the hematite to magnetite reaction is controlled by a phase boundary reaction, while the magnetite to wüstite and the wüstite to iron reaction are dominated by nucleation and growth.

4.3. Kinetic parameters

Using the models selection, the apparent reaction rates and nucleation and growth exponent can be determined. The apparent reaction rate can however be separated in the influence of the hydrogen and water vapor concentration and the influence of the temperature on the conversion rate:

$$k_{app}(T, C_{H_2}, C_{H_2O}) = k_{app}(T)\cdot(C_{H_2} - C_{H_2O}/K)^m, \quad (14)$$

in which $k_{app}(T, C_{H2}, C_{H2O})$ is the apparent reaction rate from Eq. A.1 in s^{-1}, *K* is the equilibrium constant of the reaction and C_{H2} and C_{H2O} are the hydrogen and water vapor concentration in the gas phase in mol/m^3, respectively. Due to the relatively high hydrogen flow rates used in these experiments compared to the little amount of powder, the influence of water vapor can be neglected ($C_{H2O} \approx 0$).

In the case of 500 °C (single phase boundary reaction) the dependency of the reaction on the hydrogen concentration appeared to have an order of 1.4 (exponent *m* in Eq. 13), as can be observed from the slope in Fig. 14.

For higher temperatures, the resulting gas dependency of each reaction step is shown in Fig. 15. It should be noted that for the experiments of 600 and 800 °C, only two data points are available and as such care should be taken in interpreting the results. However, the gas dependency of apparent reaction rate seems to be in the order of 1–2.5 for most cases, except for the experiment at 800 °C. Looking back at Fig. 8e, we can see that the conversion at 800 °C and a 1.0 atm. hydrogen environment completely stagnates after 40 min and does not further increase. This is most likely due to severe sintering occurring. Therefore this experiment was assumed to be faulty and the accompanied kinetic data is neglected. For the gas dependency for 400 °C and 800 °C, the results of 500 °C and the mean of 700 °C and 900 °C are assumed, respectively. A summary of the kinetic parameters obtained are presented in Table 3.

Since the exponent of the nucleation and growth model for both the magnetite to wüstite and the wüstite to iron reaction change as function of temperature, as can be seen in Table 3, it is impossible to derive a meaningful activation energy for these reactions. As mentioned before, since the hematite to magnetite reaction occurs early on in the experiment, it is intertwined with the stabilization of the hydrogen-nitrogen gas ratio and therefore no activation energy is determined.

These results described in this work provide an initial understanding in the reduction of combusted iron particles. More research is required to investigate the influence of, among others, particle size and water vapor concentration.

5. Conclusions

The reduction kinetics of iron oxides fines by hydrogen was investigated using thermogravimetric analysis in the temperature range of 400–900 °C. The powder, consisting of a mixture of hematite and magnetite, was produced by combustion of iron in air. During reduction, the removal of oxygen leads to formation of pores in the particles, and the morphology (pore size, amount of pores) of the products strongly depends on the reduction temperature. Fewer, but larger pores were observed for reduction at higher temperature. The pore morphology was found to be independent of hydrogen concentration. Mathematical modeling of the experimental data of conversion, using an extended version of the Hancock and Sharp method in combination with the model fitting method, showed that the reaction is entirely controlled by a single phase boundary reaction at 400 and 500 °C, while it must be described by a multistep mechanism at higher temperatures. The method showed that, at temperatures between 600 and 900 °C, the hematite to magnetite reaction was controlled by a phase boundary reaction, while the magnetite to wüstite and the wüstite to iron reactions were limited by nucleation and growth. The total reaction rate seems to be dependent on the gas concentration of hydrogen with a power of 1.4 at low temperatures. Noteworthy is that full conversion to metallic iron was reached faster at 500 °C than at higher temperatures. This investigation provides further understanding in iron oxide reduction with hydrogen, especially in the field of metal fuels, and provides a valuable new technique for analyzing kinetic data.

CRediT authorship contribution statement

C.J.M. Hessels: Conceptualization, Methodology, Formal analysis, Investigation, Writing – original draft, Writing – review & editing, Visualization, Funding acquisition. **T.A.M. Homan:** Conceptualization, Supervision, Funding acquisition. **N.G. Deen:** Conceptualization, Resources, Writing – review & editing, Supervision, Project administration, Funding acquisition. **Y. Tang:** Conceptualization, Methodology, Writing – review & editing, Supervision, Funding acquisition.

Declaration of Competing Interest

The authors declare that they have no known competing financial interests or personal relationships that could have appeared to influence the work reported in this paper.

Acknowledgments

The authors would like to thank Tim Spee for providing the combusted powder, the staff of the research groups Chemical Process Intensification, in particular Solomon A. Wassie, and Mechanics of Materials, in particular Marc van Maris, at Eindhoven University of Technology for sharing their thermogravimetric analyzer and scanning electron microscope, respectively. This research did not receive any specific grant from funding agencies in the public, commercial, or not-for-profit sectors.

Appendix A. Model fitting method

The result of the standard model fitting method for the cases of 500 °C, 600 °C and 700 °C can be seen in Fig. 16. Using these cases as an example, we can observe two issues with using solely this method. In the case of 500 °C both the phase boundary controlled model and the nucleation and growth model ($n \approx 1.09$) seem to fit the experimental result equally well. The selection of the correct kinetic mechanism is therefore up for interpretation.

For the cases of 600 and especially 700 °C, none of the models fit the experimental data well, suggesting that a multistep mechanism is required.

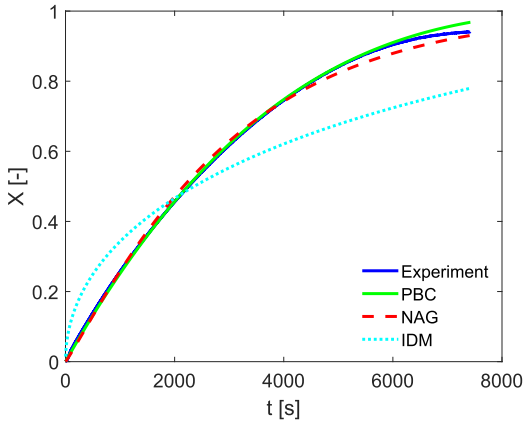

(a) Fitting results at 500°C and 0.25 atm hydrogen partial pressure.

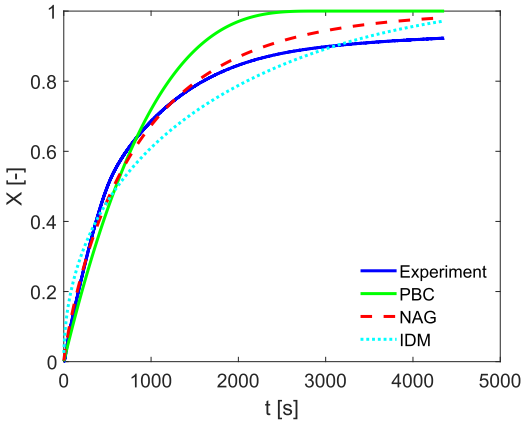

(b) Fitting results at 600°C and 0.5 atm hydrogen partial pressure.

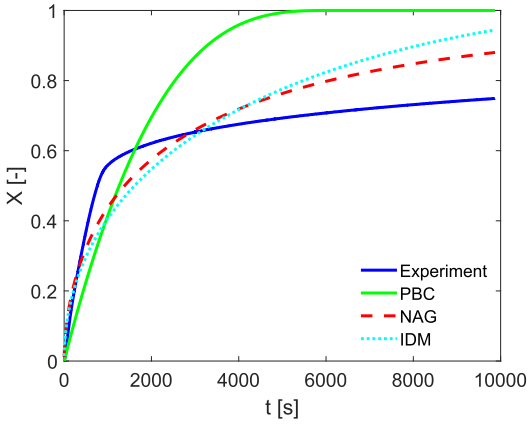

(c) Fitting results at 700°C and 0.25 atm hydrogen partial pressure.

Fig. 16. Fitting results using the model fitting method.

References

[1] H. Tanaka, Resources trend and use of directly reduced iron in steelmaking process, R and D: Res. Dev. Kobe Steel Eng. Rep. 64 (2014) 2–7.

[2] Z. Fan, S.J. Friedmann, Low-carbon production of iron and steel: technology options, economic assessment, and policy, Joule 5 (4) (2021) 829–862, https://doi.org/10.1016/j.joule.2021.02.018.

[3] V. Vogl, M. Åhman, L.J. Nilsson, Assessment of hydrogen direct reduction for fossil-free steelmaking, J. Clean. Prod. 203 (2018) 736–745, https://doi.org/10.1016/j.jclepro.2018.08.279.

[4] A. Bhaskar, M. Assadi, H. Nikpey Somehsaraei, Decarbonization of the iron and steel industry with direct reduction of iron ore with green hydrogen, Energies 13 (3) (2020), https://doi.org/10.3390/en13030758.

[5] M. Pei, M. Petäjäniemi, A. Regnell, O. Wijk, Toward a fossil free future with HYBRIT: development of iron and steelmaking technology in Sweden and Finland, Metals 10 (7) (2020), https://doi.org/10.3390/met10070972.

[6] D. Mignard, C. Pritchard, A review of the sponge iron process for the storage and transmission of remotely generated marine energy, Int. J. Hydrog. Energy 32 (18) (2007) 5039–5049, https://doi.org/10.1016/j.ijhydene.2007.06.032.

[7] J. Bergthorson, S. Goroshin, M. Soo, P. Julien, J. Palecka, D. Frost, D. Jarvis, Direct combustion of recyclable metal fuels for zero-carbon heat and power, Appl. Energy 160 (2015) 368–382, https://doi.org/10.1016/j.apenergy.2015.09.037.

[8] P. Julien, J.M. Bergthorson, Enabling the metal fuel economy: green recycling of metal fuels, Sustain. Energy Fuel 1 (2017) 615–625, https://doi.org/10.1039/C7SE00004A.

[9] L. Dirven, N.G. Deen, M. Golombok, Dense energy carrier assessment of four combustible metal powders, Sustain. Energy Technol. Assessments 30 (2018) 52–58, https://doi.org/10.1016/j.seta.2018.09.003.

[10] J.M. Bergthorson, Recyclable metal fuels for clean and compact zero-carbon power, Prog. Energy Combust. Sci. 68 (2018) 169–196, https://doi.org/10.1016/j.pecs.2018.05.001.

[11] H. Wiinikka, T. Vikström, J. Wennebro, P. Toth, A. Sepman, Pulverized sponge iron, a zero-carbon and clean substitute for fossil coal in energy applications, Energy Fuel 32 (9) (2018) 9982–9989, https://doi.org/10.1021/acs.energyfuels.8b02270.

[12] V. Spallina, H.P. Hamers, F. Gallucci, M. van Sint Annaland, Chemical Looping Combustion for Power Production Ch. 5, John Wiley and Sons, Ltd, 2015, pp. 117–174, https://doi.org/10.1002/9781118449394.ch5.

[13] Z. Wei, J. Zhang, B. Qin, Y. Dong, Y. Lu, Y. Li, W. Hao, Y. Zhang, Reduction kinetics of hematite ore fines with H2 in a rotary drum reactor, Powder Technol. 332 (2018) 18–26, https://doi.org/10.1016/j.powtec.2018.03.054.

[14] M. Elzohiery, H.Y. Sohn, Y. Mohassab, Kinetics of hydrogen reduction of magnetite concentrate particles in solid state relevant to flash ironmaking, Steel Res. Int. 10 (2016), https://doi.org/10.1002/srin.201600133.

[15] Y. Qu, Y. Yang, Z. Zou, C. Zeilstra, K. Meijer, R. Boom, Reduction kinetics of fine hematite ore particles with a high temperature drop tube furnace, ISIJ Int. 55 (5) (2015) 952–960, https://doi.org/10.2355/isijinternational.55.952.

[16] S.K. Kuila, R. Chatterjee, D. Ghosh, Kinetics of hydrogen reduction of magnetite ore fines, Int. J. Hydrog. Energy 41 (22) (2016) 9256–9266, https://doi.org/10.1016/j.ijhydene.2016.04.075.

[17] D. Spreitzer, J. Schenk, Fluidization behavior and reducibility of iron ore fines during hydrogen-induced fluidized bed reduction, Particuology 52 (2020) 36–46, https://doi.org/10.1016/j.partic.2019.11.006.

[18] K. Piotrowski, K. Mondal, T. Wiltowski, P. Dydo, G. Rizeg, Topochemical approach of kinetics of the reduction of hematite to wÃ¼stite, Chem. Eng. J. 131 (1) (2007) 73–82, https://doi.org/10.1016/j.cej.2006.12.024.

[19] R. Morales-Estrella, J. Ruiz-Ornelas, N. Ortiz-Lara, Y. Mohassab, H.Y. Sohn, Effect of mechanical activation on the hydrogen reduction kinetics of magnetite concentrate, J. Therm. Anal. Calorim. 130 (2) (2017) 713–720, https://doi.org/10.1007/s10973-017-6435-9.

[20] A. Pineau, N. Kanari, I. Gaballah, Kinetics of reduction of iron oxides by H2 part I. low temperature reduction of hematite, Thermochim. Acta 447 (1) (2006) 89–100, https://doi.org/10.1016/j.tca.2005.10.004.

[21] A. Pineau, N. Kanari, I. Gaballah, Kinetics of reduction of iron oxides by H2 part II: low temperature reduction of magnetite, Thermochim. Acta 456 (2) (2007) 75–88, https://doi.org/10.1016/j.tca.2007.01.014.

[22] P. Pourghahramani, E. Forssberg, Reduction kinetics of mechanically activated hematite concentrate with hydrogen gas using nonisothermal methods, Thermochim. Acta 454 (2) (2007) 69–77, https://doi.org/10.1016/j.tca.2006.12.023.
[23] H.-Y. Lin, Y.-W. Chen, C. Li, The mechanism of reduction of iron oxide by hydrogen, Thermochim. Acta 400 (1) (2003) 61–67, https://doi.org/10.1016/S0040-6031(02)00478-1.
[24] D. Spreitzer, J. Schenk, Reduction of iron oxides with hydrogen—a review, steel research international, 2019, p. 1900108, https://doi.org/10.1002/srin.201900108.
[25] A.Z. Ghadi, M.S. Valipour, S.M. Vahedi, H.Y. Sohn, A review on the modeling of gaseous reduction of iron oxide pellets, steel research international 91 (1) (2019) 1900270, https://doi.org/10.1002/srin.201900270.
[26] S.-H. Kim, X. Zhang, Y. Ma, I.R. Souza Filho, K. Schweinar, K. Angenendt, D. Vogel, L.T. Stephenson, A.A. El-Zoka, J.R. Mianroodi, M. Rohwerder, B. Gault, D. Raabe, Influence of microstructure and atomic-scale chemistry on the direct reduction of iron ore with hydrogen at 700°C, Acta Mater. 212 (2021) 116933, https://doi.org/10.1016/j.actamat.2021.116933.
[27] J.D. Hancock, J.H. Sharp, Method of comparing solid-state kinetic data and its application to the decomposition of kaolinite, brucite, and BaCO3, J. Am. Ceram. Soc. 55 (2) (1972) 74–77, https://doi.org/10.1111/j.1151-2916.1972.tb11213.x.
[28] T. Spee, Toward the design of a MILD cyclonic combustor (MC2) for metal fuels, Master's thesis, Eindhoven University of Technology, May 2018.
[29] J. Huang, S. Li, D. Sanned, L. Xu, S. Xu, Q. Wang, M. Stiti, Y. Qian, W. Cai, E. Berrocal, M. Richter, M. Aldén, Z. Li, A detailed study on the micro-explosion of burning iron particles in hot oxidizing environments, Combust. Flame (2021), 111755, https://doi.org/10.1016/j.combustflame.2021.111755.
[30] S. Li, D. Sanned, J. Huang, E. Berrocal, W. Cai, M. Aldén, M. Richter, Z. Li, Stereoscopic high-speed imaging of iron microexplosions and nanoparticle-release, Opt. Express 29 (21) (2021) 34465–34476, https://doi.org/10.1364/OE.434836.
[31] J. Huang, S. Li, W. Cai, Y. Qian, E. Berrocal, M. Aldén, Z. Li, Quantification of the size, 3d location and velocity of burning iron particles in premixed methane flames using high-speed digital in-line holography, Combust. Flame 230 (2021), 111430, https://doi.org/10.1016/j.combustflame.2021.111430.
[32] T. Hazenberg, J. van Oijen, Structures and burning velocities of flames in iron aerosols, Proc. Combust. Inst. 38 (3) (2021) 4383–4390, https://doi.org/10.1016/j.proci.2020.07.058.
[33] D. Ning, Y. Shoshin, J. van Oijen, G. Finotello, L. de Goey, Burn time and combustion regime of laser-ignited single iron particle, Combust. Flame 230 (2021), 111424, https://doi.org/10.1016/j.combustflame.2021.111424.
[34] D. Ning, Y. Shoshin, M. van Stiphout, J. van Oijen, G. Finotello, P. de Goey, Temperature and phase transitions of laser-ignited single iron particle, Combust. Flame 236 (2022), 111801, https://doi.org/10.1016/j.combustflame.2021.111801.
[35] J. Paleäka, J. Sniatowsky, S. Goroshin, A.J. Higgins, J.M. Bergthorson, A new kind of flame: observation of the discrete flame propagation regime in iron particle suspensions in microgravity, Combust. Flame 209 (2019) 180–186, https://doi.org/10.1016/j.combustflame.2019.07.023.
[36] M. McRae, P. Julien, S. Salvo, S. Goroshin, D.L. Frost, J.M. Bergthorson, Stabilized, flat iron flames on a hot counterflow burner, Proc. Combust. Inst. 37 (3) (2019) 3185–3191, https://doi.org/10.1016/j.proci.2018.06.134.
[37] P. Julien, S. Whiteley, S. Goroshin, M.J. Soo, D.L. Frost, J.M. Bergthorson, Flame structure and particle-combustion regimes in premixed methane–iron–air suspensions, Proc. Combust. Inst. 35 (2) (2015) 2431–2438, https://doi.org/10.1016/j.proci.2014.05.003.
[38] J. Palečka, S. Goroshin, A.J. Higgins, Y. Shoshin, P. de Goey, J.-R. Angilella, H. Oltmann, A. Stein, B. Schmitz, A. Verga, S. Vincent-Bonnieu, W. Sillekens, J. M. Bergthorson, Percolating reaction–diffusion waves (PERWAVES)—sounding rocket combustion experiments, Acta Astronautica 177 (2020) 639–651, https://doi.org/10.1016/j.actaastro.2020.07.033.
[39] E.I. Senyurt, E.L. Dreizin, At what ambient temperature can thermal runaway of a burning metal particle occur? Combust. Flame 236 (2022), 111800 https://doi.org/10.1016/j.combustflame.2021.111800.
[40] P. Tóth, Y. Ögren, A. Sepman, P. Gren, H. Wiinikka, Combustion behavior of pulverized sponge iron as a recyclable electrofuel, Powder Technol. 373 (2020) 210–219, https://doi.org/10.1016/j.powtec.2020.05.078.
[41] N. Poletaev, M. Khlebnikova, Combustion of iron particles suspension in laminar premixed and diffusion flames, Combust. Sci. Technol. 0 (0) (2020) 1–22, https://doi.org/10.1080/00102202.2020.1812588.
[42] K. Coenen, F. Gallucci, P. Cobden, E. van Dijk, E. Hensen, M., Van Sint Annaland, chemisorption working capacity and kinetics of CO2 and H2O of hydrotalcite-based adsorbents for sorption-enhanced water-gas-shift applications, Chem. Eng. J. 293 (2016) 9–23, https://doi.org/10.1016/j.cej.2016.02.050.
[43] E.T. Turkdogan, J.V. Vinters, Gaseous reduction of iron oxides: part III. Reduction-oxidation of porous and dense iron oxides and iron, Metall. Trans. A. 3 (6) (1972) 1561–1574, https://doi.org/10.1007/BF02643047.
[44] A.A. El-Geassy, M.I. Nasr, M.M. Hessien, Effect of reducing gas on the volume change during reduction of iron oxide compacts, ISIJ Int. 36 (6) (1996) 640–649, https://doi.org/10.2355/isijinternational.36.640.
[45] L. Yi, Z. Huang, T. Jiang, L. Wang, T. Qi, Swelling behavior of iron ore pellet reduced by H2–CO mixtures, Powder Technol. 269 (2015) 290–295, https://doi.org/10.1016/j.powtec.2014.09.018. https://www.sciencedirect.com/science/article/pii/S0032591014008067.
[46] Y. Qu, L. Xing, L. Shao, Y. Luo, Z. Zou, Microstructural characterization and gas-solid reduction kinetics of iron ore fines at high temperature, Powder Technol. 355 (2019) 26–36, https://doi.org/10.1016/j.powtec.2019.06.048.